

**Spin vibronics in interacting nonmagnetic molecular nanojunctions**S. Weiss,<sup>1</sup> J. Brüggemann,<sup>2</sup> and M. Thorwart<sup>2</sup><sup>1</sup>*Theoretische Physik, Universität Duisburg-Essen and CENIDE, 47048 Duisburg, Germany*<sup>2</sup>*I. Institut für Theoretische Physik, Universität Hamburg, Jungiusstraße 9, 20355 Hamburg, Germany*

(Received 13 May 2015; revised manuscript received 15 June 2015; published 27 July 2015)

We show that in the presence of ferromagnetic electronic reservoirs and spin-dependent tunnel couplings, molecular vibrations in nonmagnetic single molecular transistors induce an effective intramolecular exchange magnetic field. It generates a finite spin accumulation and precession for the electrons confined on the molecular bridge and occurs under (non)equilibrium conditions. The effective exchange magnetic field is calculated here to lowest order in the tunnel coupling for a nonequilibrium transport setup. Coulomb interaction between electrons is taken into account as well as a finite electron-phonon coupling. We show that for realistic physical parameters, an effective spin-phonon coupling emerges. It is induced by quantum many-body interactions, which are either of electron-phonon or Coulomb type. We investigate the precession and accumulation of the confined spins as function of bias and gate voltages as well as their dependence on the angle enclosed by the magnetizations between the left and right reservoir.

DOI: [10.1103/PhysRevB.92.045431](https://doi.org/10.1103/PhysRevB.92.045431)

PACS number(s): 72.25.Mk, 73.23.Hk, 73.63.Kv, 85.75.—d

**I. INTRODUCTION**

Understanding the interplay between Coulomb interaction and the coupling of the electronic charge to vibrational degrees of freedom has motivated intense research in several areas of condensed matter physics in the recent years. Transistors in future nanoelectronic applications will ideally work with only a few physical carriers of information. Inherently, the dimension of the devices are scaled down, such that response times shorten and fast switching between the two states of a transistor (or a quantum dot) becomes possible. For few-electron quantum dots, the relevant physical properties, such as the number of confined electrons, effective  $g$ -factor, and spin-orbit coupling strengths, are coherently controllable by tuning respective gate voltages in experiments (see Refs. [1,2] and references therein). Suitable physical setups include semiconducting heterostructures as well as carbon nanotubes [3] or gated nanowires [4] in order to confine a small number of electrons. Mechanical degrees of freedom are inherent to the particular geometry of these devices.

In molecular transistors (or nanojunctions), the electronic and/or spin states of a molecule are used in a controlled way to realize logical operations [5,6]. Aside from their electronic properties, molecules inherently possess significant internal vibrational degrees of freedom. Characteristic frequencies of internal mechanical vibrational modes of a molecule are used to witness a working device in a transport setup [7,8]. In general, nanomechanical systems designed by means of a clamped nanobeam, exhibit vibrational degrees of freedom as well [9]. By properly adjusting electrostatic gates, nanomechanical quantum dots with a vibrational degree of freedom are created. Depending on the particular situation, the energy scales of the electronic energies and the vibrational motion may compete and may generate rich physical phenomena. For example, electronic energies can be significantly shifted due to a strong electron-vibrational coupling. This gives rise to the Franck-Condon blockade as observed in carbon nanotubes [10], as well as a strong coupling between the tunneling of electrons and the mechanical motion [11].

In addition to controlling charge states, the electronic spin degree of freedom has been addressed as well in electronic

devices [12]. In quantum dots, electron spin resonance measurements allow to determine the particular state of the confined particle. Also in clean nanotubes, spin-orbit coupling effects serve to further split the single-particle energy spectrum in the absence of an external magnetic field. There, spin and valley degrees of freedom may be used to define appropriate qubits [3,13,14]. Since the electron spin is a natural two-state system, control and coherent manipulation of a system with a few confined spins is desirable for applications in spintronics and for encoding quantum information.

As a generic theoretical model for all the mentioned scenarios, the Anderson-Holstein model has been established in recent years. A quantum dot or a molecular nanojunction with a few electronic orbitals and a finite electron-phonon coupling is tunnel coupled to large reservoirs of free electrons. The interplay between the electronic states and the mechanical motion in Anderson-Holstein setups has been in focus recently. Franck-Condon blockade effects together with large Fano factors have been studied [15] as well as the transport properties of the system in the presence of a finite-temperature bias [15,16]. Both cases were analyzed in the weak-to-intermediate coupling regime. Thereby, tunneling processes up to second order in the dot-lead hybridization have been taken into account. For slow phonons (i.e., small phonon frequencies), the adiabatic phonon regime has been addressed [17,18]. Also in this regime, Jovchev *et al.* [19] have performed a scattering state renormalization group study in order to compute the  $I(V)$  characteristics and to determine the spectral function under the condition of thermal equilibrium. An advanced perturbative treatment of the electron-phonon coupling under nonequilibrium conditions has also been worked out [20]. Likewise, Monte Carlo simulations have been performed in the transient regime [21]. Restricting the Hilbert space to the subspace of a singly occupied electronic device, Flensberg *et al.* [22,23] have used an incoherent rate-equation approach together with the assumption that the phonon is in thermal equilibrium to reproduce the main experimental features on a qualitative level [24]. The influence on transport of a nonadiabatic phonon has been studied in Refs. [15,25]. In addition, the crossover between the regime of

the adiabatic and the weak tunneling has been addressed by the iterative summation of nonequilibrium quantum path integrals in Ref. [26], suggesting that the Franck-Condon blockade arises also at low temperatures.

Further interesting effects come into play when quantum dots are contacted by ferromagnetic leads. Then, the reservoirs can induce effective exchange magnetic fields for the electrons in the quantum dot. This has become known as the spin-valve effect. Here, the electronic spin quantum number is no longer a good quantum number, and the confined spins are allowed to precess coherently [27–29]. Ferromagnets may be characterized by their difference in the density of states of the majority and the minority spins. When two reservoirs are present (say, the left and the right one) with different magnetizations, the tunneling magnetoresistance (TMR) depends sensitively on the angle enclosed by the directions of the two magnetizations. Certainly, this opens up the possibility to manipulate spin states and initialize or read out the particular states. A proper theoretical description has to include a description of the quantum coherences appearing in the system. In the present context, quantum coherences arise due to the coherent spin evolution. A detailed study of the coherent time evolution of the electron spin in the presence of an electron-phonon coupling has not been reported so far in the literature. The influence of the electron-phonon coupling in quantum transport setups with ferromagnetic leads has been studied by means of nonequilibrium Green’s function for the two limiting cases of vanishing Coulomb interaction ( $U = 0$ ) and infinitely large Coulomb interaction ( $U \rightarrow \infty$ ) in Refs. [30,31], respectively. Also, the case of a single coupled ferromagnet used as a switch for the current polarization has been investigated recently [32]. A Hartree-Fock-type approximation is used to close the set of equations for the causal electronic Green’s functions, yielding the tunneling current and the tunneling magnetoresistance [33]. We note that within these approximations, a quantum coherent spin evolution on the quantum dot is not obtained due to the absence of inhomogeneous magnetic fields and/or approximations regarding the Coulomb interaction between electrons. In the context of nanocooling a quantum dot by spin-polarized nonequilibrium currents, a similar setup as suggested here has been investigated [34,35]. There, the focus has been on the dynamical cooling and heating of the phonon mode in presence of a *magnetic* molecular junction.

In this work, we consider a nonmagnetic molecular bridge with weak coupling to ferromagnetic leads. We include, besides the electronic degrees of freedom, also a coupling of the electrons to a single mode of a molecular vibration. Furthermore, we restrict our analysis to the sequential tunneling regime, which we explore by means of a real-time diagrammatic approach for the reduced density matrix of the molecular bridge. After introducing the ferromagnetic Anderson-Holstein model in Sec. II, we discuss the necessary modifications in the quantum kinetic equation due to the spin-polarized leads, as opposed to the case of nonmagnetic leads. Most importantly, we find an exchange magnetic field which acts on the dot electrons and which is generated by the coupling of the electrons to the vibrational mode. We discuss this effect for realistic experimental parameters in Sec. III. We calculate the relevant spin observables and discuss spin precession and

accumulation also in terms of specific elements of the reduced density matrix in Sec. IV. Transport observables (such as the charge current) for a nonequilibrium situation as well as for different polarization angles of the leads are presented in Sec. V. We show that the phonon-induced exchange magnetic field generates a current blockade which is weaker as compared to the pure spin-valve effect. To complete the physical picture, we also provide the results for the general case when both the Coulomb and the electron-phonon couplings are present. We underpin these numerical findings in terms of an attractive effective Anderson model for the polarons. We conclude and summarize our findings in Sec. VII.

## II. MODEL AND DIAGRAMMATIC TECHNIQUE

In order to model the Anderson-Holstein spin-valve geometry, we use the Hamiltonian

$$\mathcal{H} = H_{\text{mol}} + H_T + H_{\text{leads}}. \quad (1)$$

The central region [see Fig. 1(a)] is denoted as “dot,” or, equivalently, as “molecule” in what follows and may be given as, e.g., a single electronic level of a quantum dot or a molecule. Its Hamiltonian reads as ( $\hbar = 1$ )

$$H_{\text{mol}} = \sum_{\sigma} \epsilon_{\sigma} d_{\sigma}^{\dagger} d_{\sigma} + U n_{\uparrow} n_{\downarrow} + \Omega b^{\dagger} b + \lambda \hat{x} (d_{\uparrow}^{\dagger} d_{\uparrow} + d_{\downarrow}^{\dagger} d_{\downarrow}). \quad (2)$$

The fermionic operators  $d_{\sigma}$  ( $d_{\sigma}^{\dagger}$ ) annihilate (create) an electron with spin  $\sigma = \uparrow/\downarrow$  on the dot. Moreover, the electron number operator on the dot is  $n_{\sigma} = d_{\sigma}^{\dagger} d_{\sigma}$ . The single-particle energy is given by  $\epsilon_{\sigma}$  and may be controlled by an applied gate voltage and/or an external magnetic field. In the absence of an additional external magnetic field, we have that  $\epsilon_{\uparrow} = \epsilon_{\downarrow} = \epsilon_0$ . Onsite Coulomb interaction is taken into account by the parameter  $U$ . Furthermore, the vibrational mode is characterized by the bosonic operators  $b/b^{\dagger}$ , and its frequency is denoted by  $\Omega$ . The (spin-independent) electron-phonon coupling strength is provided by  $\lambda$ . The oscillator displacement operator is denoted by  $\hat{x}$ , and the harmonic eigenstates are labeled by the quantum numbers  $|m\rangle$ . In the absence of the

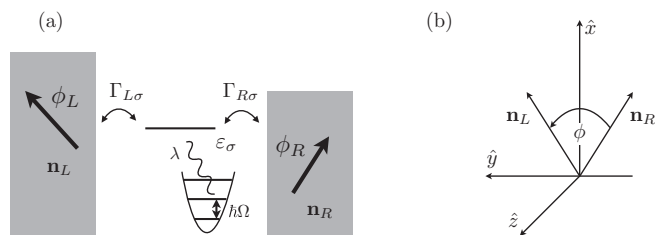


FIG. 1. (a) Sketch of the Anderson-Holstein spin-valve geometry. The spinful electronic level with energy  $\epsilon_{\sigma}$  is coupled to a single mechanical harmonic mode with frequency  $\Omega$  with a coupling constant  $\lambda$ . The electrons are able to tunnel from the spin-polarized leads to the nonmagnetic device due to finite tunneling couplings  $\Gamma_{L/R\sigma}$ . The left and right ferromagnets have different magnetizations, which are characterized by an angle  $\phi_{\alpha}$ ,  $\alpha = L/R$ . (b) The underlying coordinate system where  $\phi$  is the relative angle between the two directions  $\mathbf{n}_{L/R}$  of the left and the right magnetizations.

coupling to the phonon,  $\lambda = 0$ , the electronic eigenstates  $\{|0\rangle, |\uparrow\rangle, |\downarrow\rangle, |d\rangle\}$  correspond to the empty, the two singly, and the doubly occupied states of the quantum dot.

Spin-dependent transport features emerge due to ferromagnetic leads. We allow for different hybridizations for the up- and the down-spin electrons between the leads and the dot and describe them by the Hamiltonian

$$H_{\text{leads}} = \sum_{\mathbf{k}\alpha\tau} (\epsilon_{\mathbf{k}\tau} - \mu_{\alpha}) c_{\mathbf{k}\alpha\tau}^{\dagger} c_{\mathbf{k}\alpha\tau}. \quad (3)$$

Electrons in lead  $\alpha = L/R$  with energy  $\epsilon_{\mathbf{k}\tau}$  are created (annihilated) by the fermionic operators  $c_{\mathbf{k}\alpha\tau}^{\dagger}$  ( $c_{\mathbf{k}\alpha\tau}$ ), where  $\tau = \pm$  labels the majority/minority spin species. The quantization axis of the left and right lead, respectively, is defined by the respective magnetization directions  $\mathbf{n}_L$  and  $\mathbf{n}_R$ . Both enclose an angle  $\phi_{\alpha}$  with the  $x$ -axis [see Fig. 1(b)]. We denote by  $\mu_{\alpha}$  the electrochemical potential of the lead  $\alpha$ . Ferromagnetism is included by assuming different densities of states  $\rho_{\tau=\pm}$  at the Fermi energy for majority/minority spin electrons in the respective lead. The polarization of the ferromagnetic lead  $\alpha$  is defined by  $p_{\alpha} = \frac{\rho_{\alpha+} - \rho_{\alpha-}}{\rho_{\alpha+} + \rho_{\alpha-}}$ . For nonmagnetic leads,  $p_{\alpha} = 0$ , whereas  $p_{\alpha} = 1$  corresponds to a fully polarized lead hosting majority spins only. The dot and the leads are tunnel coupled with an amplitude  $t_{\alpha}$ , leading to the Hamiltonian [27,28]

$$H_T = \sum_{\mathbf{k}\alpha\sigma\tau} \{t_{\alpha} c_{\mathbf{k}\alpha\tau}^{\dagger} U_{\tau\sigma}^{\alpha} d_{\sigma} + \text{H.c.}\}, \quad (4)$$

where the unitary operator  $U_{\tau\sigma}^{\alpha}$  describes the rotation of the spin coordinate system of the on-dot electron to the common reference frame. As in Refs. [27,28], we choose the quantization axis for electron spins on the dot along the  $z$ -axis of the system that is spanned by  $\mathbf{e}_x = (\mathbf{n}_R + \mathbf{n}_L)/|\mathbf{n}_R + \mathbf{n}_L|$ ,  $\mathbf{e}_y = (\mathbf{n}_R - \mathbf{n}_L)/|\mathbf{n}_R - \mathbf{n}_L|$ , and  $\mathbf{e}_z = \mathbf{e}_x \times \mathbf{e}_y$  [see also Fig. 1(b)]. In passing, we note that for spinors which are rotated by an angle  $\theta$  about an axis parallel to the direction of the unit vector  $\hat{\mathbf{n}}$ , the following transformation holds:

$$e^{i(\theta/2)(\hat{\mathbf{n}} \cdot \boldsymbol{\sigma})} = \cos(\theta/2) + i \hat{\mathbf{n}} \cdot \boldsymbol{\sigma} \sin(\theta/2), \quad (5)$$

where  $\boldsymbol{\sigma} = (\sigma_x, \sigma_y, \sigma_z)$  is the vector of the Pauli matrices. Accordingly, the coordinate system is rotated by the opposite angles, such that [see Fig. 1(b)] the tunneling Hamiltonian assumes the form

$$H_T = \sum_{\mathbf{k}\alpha} t_{\alpha} [c_{\mathbf{k}\alpha+}^{\dagger} (e^{i\phi_{\alpha}/2} d_{\uparrow} + e^{-i\phi_{\alpha}/2} d_{\downarrow}) \times c_{\mathbf{k}\alpha-}^{\dagger} (-e^{i\phi_{\alpha}/2} d_{\uparrow} + e^{-i\phi_{\alpha}/2} d_{\downarrow})] + \text{H.c.} \quad (6)$$

Here, we have used two rotations in series about the  $z$ - and  $y$ -axis, respectively, such that  $U_{\tau\sigma} = e^{i(\phi_{\alpha}/2)\sigma_z} e^{i(\pi/2)\sigma_y}$ . For a finite difference in the electrochemical potentials between the left and right lead,  $eV = \mu_L - \mu_R$ , a net charge current will flow and the system is in general in a nonequilibrium situation. For  $p_{\alpha} \neq 0$ , the hybridization between the dot and the lead  $\alpha$  becomes in general spin dependent and we may introduce the tunneling coupling strength  $\Gamma_{\alpha\pm} = 2\pi |t_{\alpha}|^2 \rho_{\alpha\pm}$ . Hence, electronic states with spin  $\sigma = \uparrow/\downarrow$  acquire a finite linewidth  $\Gamma_{\alpha} = \sum_{\sigma=\pm} \Gamma_{\alpha\sigma}/2$  due to their hybridization with the reservoirs.

Before we proceed with the calculation of the nonequilibrium density matrix, we apply a polaron transformation,

such that the electrons and the phonon decouple according to  $H' = SHS^{\dagger}$  [22,36]. Here,  $S = e^{(\lambda/\Omega)(b^{\dagger}-b)\sum_{\sigma} d_{\sigma}^{\dagger} d_{\sigma}}$ . By this, the eigenenergies of the bare electronic system are shifted by the polaron energy, such that  $\epsilon_{\sigma} \rightarrow \epsilon_{\sigma} - \lambda^2/\Omega$ . Successively, also the Coulomb repulsion strength gets shifted:  $U \rightarrow U - 2\lambda^2/\Omega$ . In passing, we note that typical terms of the tunneling Hamiltonian transform under  $S$  according to  $d_{\sigma} \rightarrow d_{\sigma} e^{(\lambda/\Omega)(b^{\dagger}-b)}$  and, correspondingly for the creation operators (see Ref. [22] for the details).

Since we are interested in the physical properties of the dot in the first place, the lead and the bosonic degrees of freedom are traced out, thereby yielding the reduced density matrix of the system. In order to proceed analytically, we exploit the fact that the lead and phonon Hamiltonians are quadratic in the fermionic and bosonic operators. By performing the trace, we implicitly assume that both of these subsystems remain in thermal equilibrium, even in the presence of a finite-bias voltage. Otherwise, dynamic nonequilibrium occupations of the phonon states and/or the lead electronic states have to be explicitly taken into account as well before tracing over them. The reduced density matrix of the system in general has six nonvanishing entries and includes the coherences due to the coherent spin evolution driven by the ferromagnetic leads. By following the steps described in Refs. [37,38], we may obtain the kinetic equation for the elements of the reduced density matrix

$$\begin{aligned} \frac{d}{dt} \rho_{\chi_2}^{\chi_1}(t) = & -i \sum_{\chi} (h_{\chi_1\chi} \rho_{\chi_2}^{\chi} - h_{\chi\chi_2} \rho_{\chi}^{\chi_1})(t) \\ & + \sum_{\chi_1\chi_2} \int_{-\infty}^t dt' \Sigma_{\chi_2\chi_2}^{\chi_1\chi_1}(t, t') \rho_{\chi_1}^{\chi_2}(t'), \end{aligned} \quad (7)$$

with the irreducible self-energy kernels  $\Sigma_{\chi_2\chi_2}^{\chi_1\chi_1}(t, t')$ . They include transitions of the system between even- and odd-parity states that are induced by the tunneling Hamiltonian. The internal coherences are covered by the first term and are generated by the molecular Hamiltonian  $H_{\text{mol}}$ . They are given by the Hamiltonian matrix elements  $h_{\chi\chi'}$  of  $H_{\text{mol}}$ , with  $\chi, \chi' \in \{|0\rangle, |\uparrow\rangle, |\downarrow\rangle, |d\rangle\} \otimes |m\rangle$  of the dot-plus-phonon system in the absence of the coupling to the leads. We note that for a spin-independent electron-phonon interaction  $\lambda$ , a contribution to zeroth order in the hybridization  $\Gamma_{\alpha}$  arises, which is diagonal in the basis of the phonon.

To determine the irreducible self-energy kernels, we employ the real-time diagrammatic technique [37,38] which gives a systematic expansion of the kinetic equation in orders of  $\Gamma_{\alpha}$ . The first nonvanishing order includes all terms which change the number of electrons on the dot by one. For practical purposes, we shall include the maximal number  $n$  of states in the bosonic Hilbert space and verify convergence with respect to increasing  $n$ . Then, all  $4n$  diagonal elements of the density matrix are in general nonzero and represent the occupations of the respective polaron states of the dot. In addition, the overlap between the singly occupied states with spin up and down is finite in the presence of ferromagnetic leads [27,28]. In the presence of the vibrational degree of freedom, the appearing Fermi functions are dressed by the Franck-Condon matrix elements (see Refs. [37,38]). They

simplify if we assume the vibrational mode to be always at thermal equilibrium [15,16,22,23,36]. Then, we find

$$F_{\alpha}^{\pm}(\Omega, \epsilon) = \int_{-\infty}^{\infty} \frac{d\omega}{2\pi} f_{\alpha}^{\pm}(\omega + \epsilon) C_{\Omega}^{\pm}(\omega), \quad (8)$$

where  $C_{\Omega}^{+}(\omega) = 2\pi \sum_{n=-\infty}^{\infty} P_n(\lambda/\Omega) \delta(\omega - n\Omega)$  (see Ref. [23]) is the Fourier transform of the correlator

$$C_{\Omega}^{+}(t) = \langle e^{-(\lambda/\Omega)(b^{\dagger} e^{i\Omega t} - b e^{-i\Omega t})} e^{-(\lambda/\Omega)(b^{\dagger} - b)} \rangle. \quad (9)$$

Moreover, we have the detailed balance relation  $C^{+}(\omega) = C^{-}(\omega) e^{\beta\hbar\omega}$ . For completeness, we comment that the  $P_n(x)$  have an expansion in terms of modified Bessel functions [36]. For practical reasons, infinite sums are truncated once convergence is achieved for the observables of interest. Typically,  $n = 20$  is sufficient for large  $\lambda/\Gamma \simeq 10$  as studied in the following.

Charge current and spin expectation values are the interesting observables, which are also accessible in experimental setups. In the following, we focus on the symmetric case  $\Gamma_L = \Gamma_R$  and  $\mu_L = -\mu_R = eV/2$  as well as  $p_L = p_R = p$  and  $\phi_L = -\phi_R = \phi/2$  (a generalization is straightforward). We present results for the differential conductance  $dI/dV$  in the following, derived from the symmetrized tunneling current  $I = (I_L - I_R)/2$ , with

$$I_{\alpha}(t) = -e \frac{d}{dt} \sum_{\mathbf{k}\alpha\sigma} \langle c_{\mathbf{k}\alpha\sigma}^{\dagger} c_{\mathbf{k}\alpha\sigma} \rangle. \quad (10)$$

We note that the current operator has a similar structure as the tunneling Hamiltonian. Within the diagrammatic formalism, we have to replace a tunneling vertex by a current vertex and use the corresponding transition rates  $\Sigma_{\chi_2, \chi_2'}^{I, \chi_1, \chi_1'}(t, t')$  (for details see Ref. [38]). Information about the spin state of the system is obtained from the reduced density matrix  $\rho_{\chi}^{\chi'}$ , which is related to the vector of the average spin  $\boldsymbol{\sigma} = (\sigma_x, \sigma_y, \sigma_z)$ . We then have for the averages of the spin projections

$$\langle \sigma_x \rangle = \frac{\rho_{\downarrow}^{\uparrow} + \rho_{\uparrow}^{\downarrow}}{2}, \quad \langle \sigma_y \rangle = i \frac{\rho_{\downarrow}^{\uparrow} - \rho_{\uparrow}^{\downarrow}}{2}, \quad \langle \sigma_z \rangle = \frac{\rho_{\uparrow}^{\uparrow} - \rho_{\downarrow}^{\downarrow}}{2}. \quad (11)$$

### III. EXCHANGE MAGNETIC FIELD

Ferromagnetic leads induce a coherent spin dynamics on the dot although the quantum dot itself is nonmagnetic. In lowest order in the lead-dot tunneling coupling, a contribution to an effective exchange magnetic field is generated from each of the two leads. It points in the respective direction of the lead magnetization. We follow the derivation in Refs. [27,28] and explore the fact that the charge as well as the spin degrees of freedom obey rate equations. The dynamics of the spin can be formulated in terms of a time-evolution equation for the spin vector  $\boldsymbol{\sigma}(t)$  which describes the dynamics of the spin of the confined electron. This vector equation can be decomposed into three parts according to

$$\frac{d\boldsymbol{\sigma}}{dt} = \left( \frac{d\boldsymbol{\sigma}}{dt} \right)_{\text{acc}} + \left( \frac{d\boldsymbol{\sigma}}{dt} \right)_{\text{rel}} + \left( \frac{d\boldsymbol{\sigma}}{dt} \right)_{\text{rot}}, \quad (12)$$

where accumulation, relaxation, and rotation of the spin are identified by the three terms. Correspondingly, the dynamical equation of motion for the charge degrees of freedom can be

decomposed in a similar manner. As opposed to Refs. [27,28], all energies or differences of energies between singly and doubly occupied states have to be replaced by the corresponding energies of the respective polaron states (see Sec. II). A closer look to the third term in Eq. (12) yields the representation

$$\left( \frac{d\boldsymbol{\sigma}}{dt} \right)_{\text{rot}} = \boldsymbol{\sigma} \times (\mathbf{B}_L + \mathbf{B}_R) \quad (13)$$

in terms of an effective exchange magnetic field with the contributions  $\mathbf{B}_{\alpha}$  [28]. It is well known that for standard spin valves without a vibrational mode, the Coulomb interaction  $U$  between electrons can generate a finite exchange magnetic field [see Eq. (14) for  $\lambda = 0$ ]. In presence of the electron-phonon coupling, the vibrational coupling generates an effective attractive Coulomb interaction. In turn, the resulting exchange magnetic field depends on  $\lambda$  as well as on  $U$ . Overall, we find the analytic expression for the exchange magnetic field

$$\mathbf{B}_{\alpha} = -\frac{p_{\alpha}\Gamma_{\alpha}}{\pi} \left[ \Lambda_{\alpha} \left( \epsilon - \frac{\lambda^2}{\Omega} \right) - \Lambda_{\alpha} \left( \epsilon + U - \frac{3\lambda^2}{\Omega} \right) \right] \mathbf{n}_{\alpha}, \quad (14)$$

which acts from contact  $\alpha$  on the spin of the electron confined on the dot. Here,  $\Lambda_{\alpha}(x) = \text{Re} \Psi[1/2 + i\beta(x - \mu_{\alpha})/(2\pi)]$ , with the digamma function  $\Psi$  [39]. It is important to realize that even in the absence of the Coulomb interaction, i.e., for  $U = 0$ , a finite exchange field  $\mathbf{B}_{\alpha}$  in the direction  $\mathbf{n}_{\alpha}$  of the magnetization of the lead  $\alpha$  exists when an electron-phonon coupling is present  $\lambda \neq 0$ . Consequently, the spin of a confined electron, which is subject to electron-phonon coupling, will precess in the effective exchange magnetic field generated when  $\lambda \neq 0$ . Equation (14) includes previous results in the case of  $\lambda = 0$ . Furthermore, it is interesting to realize that for Coulomb interaction strengths  $U < 2\lambda^2/\Omega$ , the exchange magnetic field points into the direction opposite to that of the lead magnetization. Moreover, it vanishes exactly when  $U = 2\lambda^2/\Omega$ . The exchange magnetic field is shown in Fig. 2 as a function of the bias and the gate voltages in a color scale plot in units of  $\Gamma$  for three different cases. In Fig. 2(a), only pure Coulomb interaction is present while the electron-phonon coupling is switched off ( $U = 30k_B T$ ,  $\lambda = 0$ ). In turn, in Fig. 2(b), only pure electron-phonon interaction is present while the Coulomb term is absent ( $U = 0$ ,  $\lambda = 10k_B T$ ). Here, we have chosen the frequency of the oscillator as  $\Omega = 5k_B T$ . Finally, in Fig. 2(c), both interactions are present ( $U = 30k_B T$ ,  $\lambda = 10k_B T$ ). In the presence of the Coulomb interaction alone and for a fixed bias voltage, the exchange field shows sharp resonances. In-between these resonances, the field decreases, goes through zero, reverses its sign, and increases again to the adjacent resonance in Fig. 2(a). For pure electron-phonon coupling and in absence of a Coulomb interaction  $U = 0$  [see Fig. 2(b)], the analogy to an effective attractive Coulomb interaction appears in two respects: First, there is a finite exchange field induced by the phonon on the dot. Second, as opposed to Fig. 2(a) it has a reversed sign. As in Fig. 2(a), we find two resonances, which are shifted to higher values of  $\epsilon_0$  here. This is a general feature which is due to the opposite sign of the effective Coulomb interaction constant. In Fig. 2(c), the parameters are chosen such that  $\lambda^2/\Omega \approx U$ . The exchange magnetic field is still



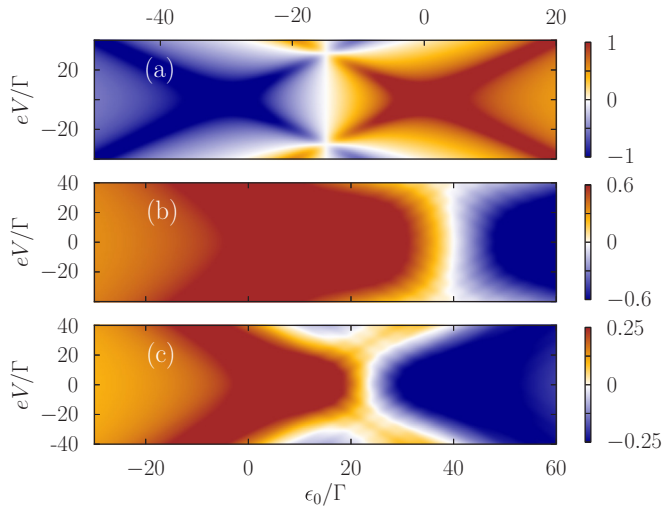


FIG. 2. (Color online) Effective exchange magnetic field in units of  $\Gamma$  induced by the electron-phonon and Coulomb interaction. The color scale shows the sum  $B_{\text{ex}} = B_L + B_R$ . Panel (a) shows the result for pure Coulomb interaction  $U = 30k_B T$  without electron-phonon coupling  $\lambda = 0$ . In (b), the electron-phonon coupling is set to  $\lambda = 10k_B T$ ,  $\Omega = 5k_B T$ , while  $U = 0$ . The finite  $\lambda$  broadens the resonances, shifts it to larger values of the gate voltage, and reverses its direction as compared to panel (a). In (c), both interactions are present. The remaining parameters are  $k_B T = \Gamma$ ,  $\phi = \pi/2$ , and  $p = 0.9$ .

visible, although being smaller in amplitude as opposed to Fig. 2(a). The width of the resonance is broader than in Fig. 2(a) which reflects the dominance of  $\lambda$ . For those parameters, we have that  $\lambda^2/\Omega > U/2$  and the tendency is as in Fig. 2(b). In contrast, the choice  $U/2 > \lambda^2/\Omega$  would result in a reversed direction of the effective exchange field again. In what follows, we discuss how the results are modified in comparison to the case  $U \neq 0$ ,  $\lambda = 0$  by a finite electron-phonon coupling.

#### IV. SPIN PRECESSION AND SPIN ACCUMULATION

The immediate consequence of the interaction-induced exchange magnetic field is a spin accumulation and spin precession of single-electron spins on the dot. Whenever the dot is doubly occupied, these effects are expected to be less pronounced since the spin-singlet state is not sensitive to inhomogeneous magnetic fields. Spin measurements have been performed in order to determine the strength of the exchange magnetic field, e.g., in carbon nanotubes contacted by ferromagnetic leads [40]. In the following, we address the spin expectation values along the three spatial directions with the coordinate system being defined as indicated in Fig. 1(b). We show results for the angle  $\phi = \pi/2$  between the left and right magnetization directions. This corresponds to the configuration  $\mathbf{n}_L \perp \mathbf{n}_R$ . From Refs. [27,28] it is known that for small bias voltages, a finite spin accumulation occurs along the direction  $\mathbf{n}_L - \mathbf{n}_R = \mathbf{e}_y$ . It also occurs in the absence of the exchange field. It is important to realize that a finite  $\langle \sigma_x \rangle \neq 0$  and/or  $\langle \sigma_z \rangle \neq 0$  is a clear signature of a finite exchange field generated by Coulomb or electron-phonon interactions.

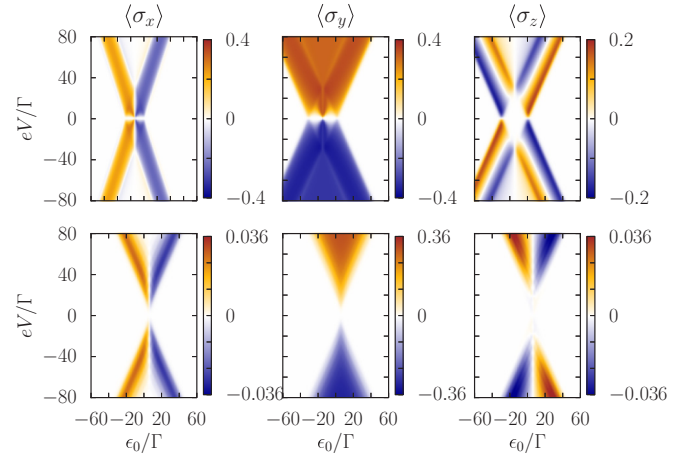


FIG. 3. (Color online) Interaction-induced spin accumulation illustrated by the spin expectation values  $\langle \sigma_x \rangle$  (left column),  $\langle \sigma_y \rangle$  (middle column), and  $\langle \sigma_z \rangle$  (right column) for varying bias and gate voltages and for  $U = 30k_B T$ . The upper row shows the results for pure Coulomb interaction without electron-phonon coupling  $\lambda = 0$ . The lower row refers to the case with an additional electron-phonon interaction  $\lambda = 10k_B T$ ,  $\Omega = 5k_B T$ . The remaining parameters are as in Fig. 2.

The induced spin accumulation is illustrated in Fig. 3 by the spin expectation values  $\langle \sigma_x \rangle$ ,  $\langle \sigma_y \rangle$ , and  $\langle \sigma_z \rangle$  for varying bias and gate voltages. The upper row shows the results for the case of pure Coulomb interaction  $U = 30k_B T$  and  $\lambda = 0$ . For  $\phi = \pi/2$ , spin is accumulated in the direction  $\mathbf{n}_L - \mathbf{n}_R$  due to the conservation of the total angular momentum. This maximal spin-valve effect competes with the spin precession around the induced exchange field which points in the direction  $\mathbf{n}_L + \mathbf{n}_R$ . The latter induces finite  $x$ - and  $z$ -component of the spin. Since two addition energies are present, also two distinct resonance lines appear in the upper left panel. The same substructure also emerges in the upper middle panel. In this case, the transitions on the dot between the states  $|\uparrow\rangle$  and  $|\downarrow\rangle$  and the empty or doubly occupied state are nondegenerate due to the finite spin accumulation. In the lower row of Fig. 3, we depict the results for  $U = 10k_B T$  and  $\lambda = 10k_B T$  which illustrate the modification of the spin accumulation and the spin precession due to a finite electron-phonon coupling  $\lambda$ . They are in accordance with Fig. 2(c), where a finite exchange field is shown. Although the spin expectation values are about one order of magnitude smaller than the exchange field, the qualitative physical behavior is the same. The electrons couple to the phonon mode differently depending on their spin due to the lead polarization. By this, an effective spin-phonon coupling emerges. On the other hand, the electron-phonon coupling compensates the repulsive Coulomb interaction and allows the dot to be occupied by two electrons.

#### Angular dependence

The choice of two independent magnetizations in the left and right lead, characterized by the relative angle  $\phi$ , generates two noncollinear magnetic fields for the spin of an electron on the dot. When the dot is occupied by a single electron, the spin state is sensitive to these fields. Then, also the

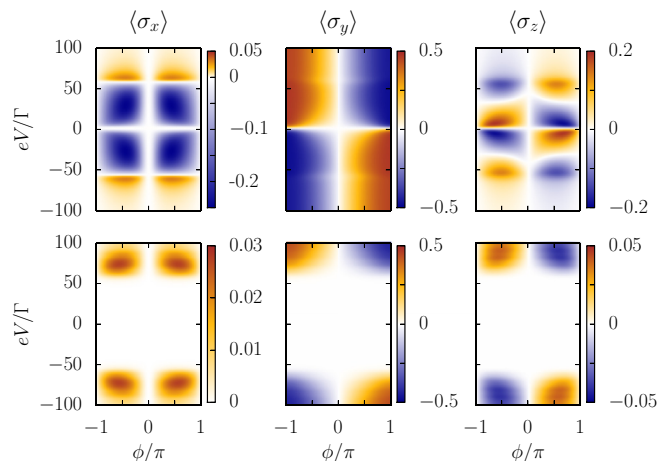


FIG. 4. (Color online) Same as in Fig. 3, but as a function of the enclosed angle  $\phi$  for a single-particle energy  $\epsilon_0 = 30k_B T$  and for  $U = 30k_B T$ . The upper row shows the results for  $\lambda = 0$ , while the lower row shows the case with an additional electron-phonon interaction  $\lambda = 10k_B T$ ,  $\Omega = 5k_B T$ .

dependence of the spin accumulation on  $\phi$  is relevant. In Fig. 4, we show the spin expectation values as a function of the bias voltage and the enclosed angle  $\phi$ . We have fixed the gate voltage to  $\epsilon_0 = 30k_B T$  and the remaining parameters are as in Fig. 3. Again, the three upper panels refer to pure repulsive Coulomb interaction with  $U > 0$ . The device is largely singly occupied and we find a clear precession of the spin with finite  $x$ - and  $z$ -component of the spin operator. In contrast to the spin accumulation, the spin precession vanishes for the collinear configurations, when  $\phi = 0, \pm\pi$ . As the spin-dependent effects are absent for zero bias voltage, we find that increasing the bias voltage favors a specific spin direction, either up or down. This is accompanied by the precession of the spin with the same or the opposite components of the spin vector. This is depicted in the left and right panels of the upper row in Fig. 4. The results for finite  $\lambda$  are shown in the lower row. The spin accumulation is sensitive to the change of the angle as well, similar as the behavior discussed above. However, the characteristics of the precession is different since it is determined by the value of the exchange magnetic field. We note that always a positive  $x$ -component of the spin emerges, whereas the  $z$ -component may reverse its sign, when either the angle or the bias voltage are changed from positive to negative values. Since the Franck-Condon blockade is well developed in the central areas of the panels, spins of any kind are blocked to enter the dot in this regime. Hence, neither spin accumulation nor spin precession occurs here.

## V. TRANSPORT SPECTROSCOPY

Measurements of the current give precise insight into the spectrum of the interacting quantum dot. In this section, we present results for the differential conductance  $dI/dV$ , with the current defined in Eq. (10). The differential conductance as function of  $eV$  and  $\epsilon_0$  is shown in Fig. 5(a) for  $U = 0$ ,  $\lambda = 0$ ,  $\Gamma = k_B T$ , and  $\phi = \pi/2$ . A single conductance line is visible since the system possesses only one addition energy  $E_{\text{add}} = \epsilon_{|\uparrow/\downarrow} - \epsilon_{|\uparrow/\downarrow} = \epsilon_{|\uparrow/\downarrow} - \epsilon_{|0} = \epsilon_0$ . The finite conductance is

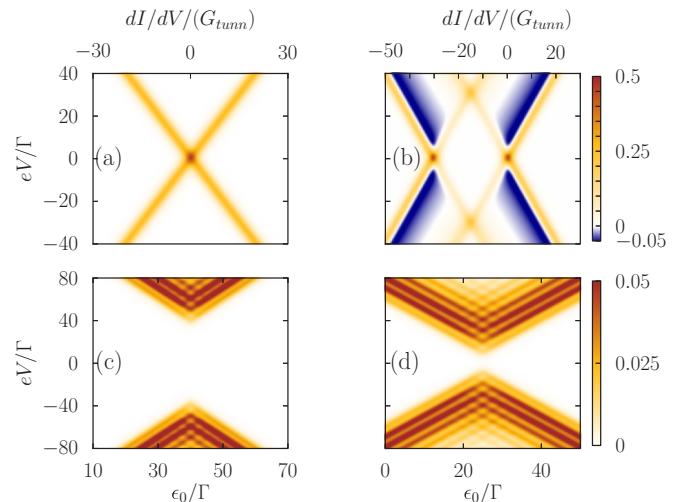


FIG. 5. (Color online) Differential conductance of the Anderson-Holstein spin valve as a function of the bias and the gate voltage in units of  $G_{\text{tunn}} = (e^2/h)\Gamma/(2\pi k_B T)$ . In (a), the noninteracting case is shown:  $U = \lambda = 0$ , while (b) refers to  $U = 30k_B T$ ,  $\lambda = 0$ . In panel (c), we set  $U = 0$ ,  $\lambda = 10k_B T$ , and in (d), we have chosen  $U = 30k_B T$ ,  $\lambda = 10k_B T$ ,  $\Omega = 5k_B T$ . All calculations have been performed with  $\Omega = 5k_B T$ ,  $p = 0.9$ , and  $\phi = \pi/2$ .

accompanied by the inset of the spin accumulation on the dot (see the discussion related to Fig. 3). In Fig. 5(b), we depict the result for  $U = 30k_B T$ ,  $\lambda = 0$ . Without the ferromagnetic leads, two addition energies exist in this case,  $\epsilon_0$  and  $\epsilon_0 + U$ . Then, for  $\epsilon_0 \leq 10\Gamma$ , the dot is in the doubly occupied state, whereas for increasing gate voltages, the singly occupied state is favored. This gives rise to the diamond in the center region of Fig. 5(b). For large gate voltages  $\epsilon_0 \gtrsim 30\Gamma$ , the dot is empty again. The linewidths are determined by the temperature, and we find pronounced satellite lines with negative values. This negative differential conductance originates from a partial blocking of spins, a competition between spin accumulation and interaction-induced spin precession. Spin accumulation hinders electrons, which do not have the right spin projection, to enter the drain, whereas spin precession counteracts to lift the blockade. The specific positions of the lines are obtained from the shape of the induced exchange field (see the discussion in Sec. III). With the lead magnetizations chosen such that  $\phi = \pi/2$ , a maximal spin-valve effect is present. The charge degeneracy points are located at  $\pm\epsilon_0 = -U/2$ , where a maximal current flows. In Fig. 5(c), we show a typical Franck-Condon differential conductance. There is a large range of bias and gate voltages ( $|eV| \leq 40k_B T$ ,  $30k_B T \leq |\epsilon_0| \leq 50k_B T$ ), where transport is largely blocked. Once the bias voltage provides enough energy, which is of the order of the polaron energy  $\lambda^2/\Omega$ , electrons are able to tunnel through the dot and a current can flow. We see equidistant lines in the spectrum that are associated with the energy differences between neighboring states. The regular appearance could be explained in terms of Franck-Condon parabolas that allow or forbid transitions from one vibrational state to another, when at the same time the number of electrons is changed [15,22,23]. Due to the polaronic energy shift  $\epsilon_0 \rightarrow \epsilon_0 + \lambda^2/\Omega$ , charge-state degeneracies are shifted differently as compared to the

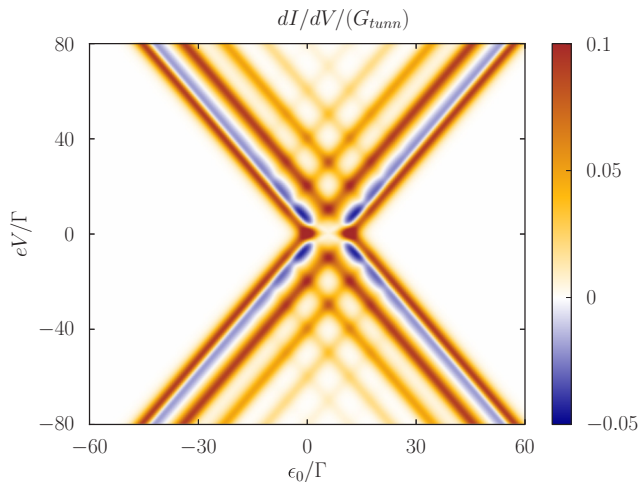


FIG. 6. (Color online) Differential conductance in the crossover regime (see text) for  $U = 30k_B T$ ,  $\lambda = \Omega = 10k_B T$ . The remaining parameters are as in Fig. 5.

situation shown in Fig. 5(b). In particular, the shift occurs to positive values of  $\epsilon_0$ . The effective attractive Coulomb interaction tends to put the dot in the doubly occupied state. Clearly, features of a negative differential conductance as in Fig. 5(b) are absent then. In Fig. 5(d), we depict results for the scenario that both interactions are finite, i.e.,  $U = 30k_B T$  and  $\lambda = 10k_B T$ . For this particular choice of parameters, the polaron energy approximately equals the Coulomb repulsion and we obtain a competition between the effects of the regimes described in Figs. 5(b) and 5(c). The parameters are  $\lambda = \Omega = 10k_B T$ ,  $U = 30k_B T$ . Decreasing the polaron energy further results in a crossover to the behavior shown in Fig. 5(b). There, the negative differential conductance is fully developed, whereas the Franck-Condon steps vanish successively. In Fig. 6, we depict the results for the crossover regime, where we find a superposition of modulated negative differential conductance lines (blue) and Franck-Condon steps in the  $dI/dV$  curve.

#### Angular dependence

The transport spectrum  $dI/dV$  as a function of the noncollinearity of the lead magnetizations  $\phi$  is shown for a fixed gate voltage  $\epsilon_0 = 30k_B T$  in Fig. 7. For a vanishing electron-phonon coupling,  $dI/dV(\phi, eV)$  for  $\lambda = 0$  is shown in Fig. 7(a). The dot is essentially unoccupied. The symmetry of the figure is due to the symmetry of the underlying setup, and we recall that we calculate the symmetrized current. For small bias voltages, a positive conductance peak appears for varying  $\phi$ . Along  $\phi$ , we recover the known suppression of the conductance away from the maximum according to  $\sin^2 \phi$  (see Refs. [27,28]). With increasing bias voltage, the dot is more populated. Depending on the noncollinearity, spin is accumulated on the dot and precesses. Transport is then reduced, and hence, a clear negative differential conductance feature occurs. For even larger bias voltages, transport is independent of  $\phi$ . In Fig. 7(b), we show the results for  $U = 30k_B T$  and  $\lambda = 10k_B T$ . Again, conductance lines are symmetric with respect to  $\phi = 0$ ,  $eV = 0$ , and the

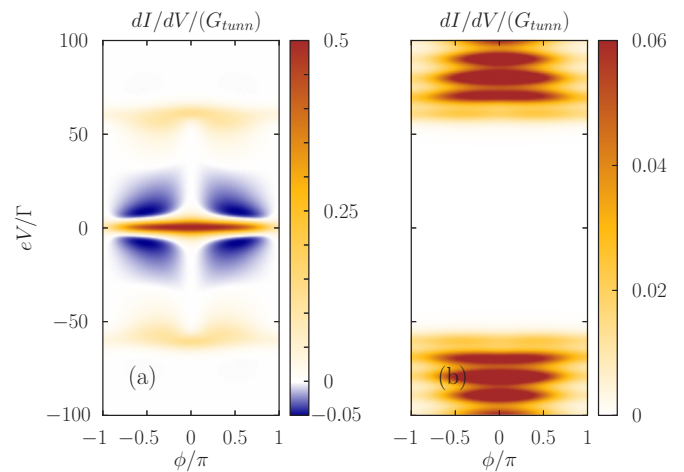


FIG. 7. (Color online) Angular dependence of the differential conductance for  $U = 30k_B T$  without electron-phonon coupling  $\lambda = 0$  in (a), and with  $\lambda = 10k_B T$ ,  $\Omega = 5k_B T$  in (b). The remaining parameters are as in Fig. 5.

strong Franck-Condon blockade is independent of the enclosed angle. Since the electron-phonon coupling favors a doubly occupied dot state, a spin-singlet state is formed. This singlet is independent of any magnetic field and thus is not influenced by changes of the angle of the lead magnetizations. As a function of  $\phi$ , the respective lines show a maximum for  $\phi = 0$ , and the reduction follows again a  $\sim \sin^2 \phi$  functional form.

#### VI. NONEQUILIBRIUM PHONON MODE

In the discussion above, we have assumed that the phonon mode is always kept at thermal equilibrium. In this section, we address the situation when this no longer holds and the phonon mode is treated fully nonadiabatically. Starting from the Hamiltonian in Eq. (2), we have to truncate the phonon Hilbert space at a certain number  $K$  of energy eigenstates. When calculating the kernels within the real-time diagrammatic approach, we explicitly keep the dependence on these basis states. Clearly, the truncation of phonon absorption and emission processes becomes increasingly cumbersome for large electron-phonon coupling. Especially in the context of cooling or heating the environment (see Ref. [34]), the full density matrix of the electron and phonon degrees of freedom is of importance in order to monitor the effective temperature which refers to the mean energy contained in the vibrational mode. In order to include nonequilibrium effects in the phonon subspace, we trace over the bosonic degrees of freedom only when we compute electronic observables, such as the current or the spin expectation values. Otherwise, we keep the  $(4K)^2$  elements of the density matrix of the dot. We show in Fig. 8(a) the differential conductance as a function of the bias voltage for  $\lambda = 2.5\Gamma$ ,  $\Omega = 5\Gamma$ ,  $k_B T = \Gamma$ ,  $U = 30\Gamma$ , and  $\epsilon = -40\Gamma$ . The solid line refers to the results with the assumption of a thermally equilibrated phonon, whereas the dashed lines mark the results for different numbers of phonon states that are taken into account. The red (blue) line is for  $K = 9$  ( $K = 10$ ) phonon states. We find a good agreement for small to intermediate bias voltages  $0 \leq |eV| \leq 30\Gamma$ . Small



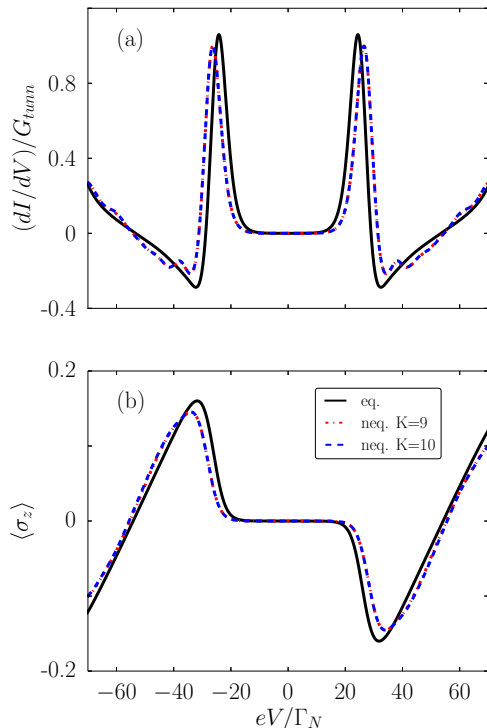


FIG. 8. (Color online) (a) Comparison of the differential conductance for equilibrated and nonequilibrated phonon modes. Within a voltage range  $|eV| \leq 20\Gamma$  we do not find significant deviations from the calculation where the phonon is assumed to be in equilibrium. (b) Same as in (a) but for the nontrivial spin projection along the  $z$ -axis. We note that  $\langle \sigma_z \rangle \neq 0$  reflects the finite exchange magnetic field from the leads. Other parameters are chosen as  $\lambda = 2.5\Gamma$ ,  $k_B T = \Gamma$ ,  $\phi = \pi/2$ ,  $\Omega = 5\Gamma$ ,  $\epsilon = -40\Gamma$ .

side peaks develop at larger bias voltages, which are associated to the influence of the nonequilibrium phonon distribution. However, the key features, such as the appearance of the negative differential conductance and the Lorentzian peaks at  $|eV| = U/2 + \lambda^2/\Omega$  are reproduced by the equilibrium phonon distribution as well. The height of the peaks differs to some extent between the equilibrium and the nonequilibrium phonon model. For larger values of  $\lambda > 3\Gamma$ , it is difficult to obtain numerically converged results and the calculation in the Franck-Condon regime becomes increasingly cumbersome. In Fig. 8(b), we compare, as an example, the  $z$ -component of the spin for both models. Again, the qualitative form of the spin expectation value as a function of the bias voltage agrees for both types of calculations, apart from small deviations and different peak heights.

## VII. CONCLUSIONS

The interplay of ferromagnetism, Coulomb and electron-phonon coupling in quantum dots or molecular transistors gives rise to interesting spintronic effects under nonequilibrium conditions. In the presence of ferromagnetic leads, the nonmagnetic molecular bridge supports a coherent time evolution of the spin between the  $|\uparrow\rangle$  and  $|\downarrow\rangle$  states. When the tunnel coupling is weak, we obtain the stationary density matrix in the presence of a finite bias voltage by means of the real-time diagrammatic technique. Thereby, we include all quantum coherences that govern the coherent evolution of the confined electron spin. As a central result, we find a phonon-induced exchange magnetic field which acts on the electron spins confined in the intrinsically nonmagnetic dot. The electron-phonon coupling induces an effective attractive Coulomb interaction, which, together with the spin-valve effect, induces a precession of the confined electron spins in the dot. Interestingly enough, we find that the induced exchange magnetic field points in the opposite direction when  $\lambda \neq 0$ , as compared to  $U \neq 0$ . The phonon-induced exchange field shows much broader resonances than the Coulomb-induced exchange field. This behavior is related to the small energy spacings between the adjacent energy levels in the polaron picture. However, once a single spin is confined on the dot, it starts to precess in the effective exchange field. When  $\lambda$  is finite, Franck-Condon physics emerges. In particular, the Franck-Condon blockade gives rise to an empty dot, and counteracts the spin-valve physics. Nevertheless, if both interactions are of the same order of magnitude, spin-valve physics survives, and spin accumulation together with a spin precession is observable. These effects are to some extent weaker as compared to the standard pure spin-valve scenario. Also, the symmetrized tunneling current and the differential conductance are accessible. In addition to the known results for the conventional quantum dot spin valve and the established Franck-Condon sidebands, we propose a combined  $dI/dV$  diagram, where the negative differential properties of the quantum dot spin valve are modulated by the Franck-Condon sidebands. These theoretically proposed effects might be observable in ultraclean carbon nanotubes or gated single-molecule setups, for instance, by magnetic scanning tunneling microscope experiments in the near future.

## ACKNOWLEDGMENTS

We thank J. König, P. Stegmann, and P. Nalbach for fruitful discussions. Financial support by the DFG Schwerpunktprogramm ‘‘Spin Caloritronics’’ (SPP 1538) for J.B. and by the DFG Sonderforschungsbereich 668 ‘‘Magnetismus vom Einzelatom zur Nanostruktur’’ is acknowledged as well.

- [1] R. Hanson, L. P. Kouwenhoven, J. R. Petta, S. Tarucha, and L. M. K. Vandersypen, *Rev. Mod. Phys.* **79**, 1217 (2007).  
 [2] W. G. van der Wiel, S. d. Franceschi, J. M. Elzerman, T. Fujisawa, S. Tarucha, and L. P. Kouwenhoven, *Rev. Mod. Phys.* **75**, 1 (2003).

- [3] E. A. Laird, F. Kuemmeth, G. Steele, K. Grove-Rasmussen, J. Nygard, K. Flensberg, and L. P. Kouwenhoven, [arXiv:1403.6113](https://arxiv.org/abs/1403.6113) [Rev. Mod. Phys. (to be published)].  
 [4] I. Shorubalko, A. Pfund, R. Leturcq, M. T. Borgström, F. Gramm, E. Müller, E. Gini, and K. Ensslin, *Nanotechnology* **18**, 044014 (2007).



- [5] N. A. Zimbovskaya and M. R. Pederson, *Phys. Rep.* **509**, 1 (2011).
- [6] J. C. Cuevas and E. Scheer, *Molecular Electronics: An Introduction to Theory and Experiment* (World Scientific, Singapore, 2010).
- [7] M. Galperin, M. A. Ratner, and A. Nitzan, *J. Phys.: Condens. Matter* **19**, 103201 (2007).
- [8] O. Tal, M. Krieger, B. Leerink, and J. M. van Ruitenbeek, *Phys. Rev. Lett.* **100**, 196804 (2008).
- [9] H. G. Craighead, *Science* **290**, 1532 (2000); M. L. Roukes, *Phys. World* **14**, 25 (2001).
- [10] R. Leturcq, C. Stampfer, K. Inderbitzin, L. Durrer, C. Hierold, E. Mariani, M. G. Schultz, F. von Oppen, and K. Ensslin, *Nat. Phys.* **5**, 327 (2009).
- [11] G. A. Steele, A. K. Hüttl, B. Witkamp, M. Poot, H. B. Meerwaldt, L. P. Kouwenhoven, and H. S. J. van der Zant, *Science* **325**, 1103 (2009).
- [12] I. Zutic, J. Fabian, and S. Das Sarma, *Rev. Mod. Phys.* **76**, 323 (2004).
- [13] S. Weiss, E. I. Rashba, F. Kuemmeth, H. O. H. Churchill, and K. Flensberg, *Phys. Rev. B* **82**, 165427 (2010).
- [14] H. O. H. Churchill, F. Kuemmeth, J. W. Harlow, A. J. Bestwick, E. I. Rashba, K. Flensberg, C. H. Stwertka, T. Taychatanapat, S. K. Watson, and C. M. Marcus, *Phys. Rev. Lett.* **102**, 166802 (2009).
- [15] J. Koch and F. von Oppen, *Phys. Rev. Lett.* **94**, 206804 (2005).
- [16] M. Leijnse, M. R. Wegewijs, and K. Flensberg, *Phys. Rev. B* **82**, 045412 (2010).
- [17] F. Pistolesi, Ya. M. Blanter, and I. Martin, *Phys. Rev. B* **78**, 085127 (2008).
- [18] N. Bode, S. V. Kusminskiy, R. Egger, and F. von Oppen, *Phys. Rev. Lett.* **107**, 036804 (2011).
- [19] A. Jovchev and F. B. Anders, *Phys. Rev. B* **87**, 195112 (2013).
- [20] R. Egger and A. O. Gogolin, *Phys. Rev. B* **77**, 113405 (2008).
- [21] K. F. Albrecht, H. Wang, L. Mühlbacher, M. Thoss, and A. Komnik, *Phys. Rev. B* **86**, 081412(R) (2012).
- [22] K. Flensberg, *Phys. Rev. B* **68**, 205323 (2003).
- [23] S. Braig and K. Flensberg, *Phys. Rev. B* **68**, 205324 (2003).
- [24] H. Park, J. Park, A. K. L. Lim, E. H. Anderson, A. P. Alivisatos, and P. L. McEuen, *Nature (London)* **407**, 57 (2000).
- [25] A. Mitra, I. Aleiner, and A. J. Millis, *Phys. Rev. B* **69**, 245302 (2004).
- [26] R. Hütten, S. Weiss, M. Thorwart, and R. Egger, *Phys. Rev. B* **85**, 121408(R) (2012).
- [27] J. König and J. Martinek, *Phys. Rev. Lett.* **90**, 166602 (2003).
- [28] M. Braun, J. König, and J. Martinek, *Phys. Rev. B* **70**, 195345 (2004).
- [29] L. Balents and R. Egger, *Phys. Rev. Lett.* **85**, 3464 (2000).
- [30] Zuo-Zi Chen, Rong Lü, and Bang-fen Zhu, *Phys. Rev. B* **71**, 165324 (2005).
- [31] Rui-Qiang Wang, Yun-Qing Zhou, Beigang Wang, and D. Y. Xing, *Phys. Rev. B* **75**, 045318 (2007).
- [32] Y. Guo, J. Zheng, and F. Chi, *J. Low Temp. Phys.* **174**, 145 (2014).
- [33] W. Rudzinski, *J. Phys.: Condens. Matter* **20**, 275214 (2008).
- [34] J. Brüggemann, S. Weiss, P. Nalbach, and M. Thorwart, *Phys. Rev. Lett.* **113**, 076602 (2014).
- [35] P. Stadler, W. Belzig, and G. Rastelli, *Phys. Rev. Lett.* **113**, 047201 (2014).
- [36] G. D. Mahan, *Many-Particle Physics* (Plenum, New York, 1990).
- [37] J. König, J. Schmid, H. Schoeller, and G. Schön, *Phys. Rev. B* **54**, 16820 (1996).
- [38] B. Sothmann and J. König, *Phys. Rev. B* **82**, 245319 (2010).
- [39] I. S. Gradshteyn and I. M. Ryzhik, *Table of Integrals, Series and Products* (Academic, New York, 2000).
- [40] J. R. Hauptmann, J. Paaske, and P. E. Lindelof, *Nat. Phys.* **4**, 373 (2008).